

Observations of Island Wakes at High Rossby Numbers: Evolution of Submesoscale Vortices and Free Shear Layers

MING-HUEI CHANG, SEN JAN, CHIH-LUN LIU, AND YU-HSIN CHENG

Institute of Oceanography, National Taiwan University, Taipei, Taiwan

VIGAN MENSAH

Institute of Oceanography, National Taiwan University, Taipei, Taiwan, and Institute of Low Temperature Science, Hokkaido University, Hokkaido, Japan

(Manuscript received 9 February 2019, in final form 4 September 2019)

ABSTRACT

Oceanic vortex evolution on the lee side of Taiwan's Green Island (~ 7 km in diameter), where the Kuroshio flows at a speed of $1\text{--}1.5\text{ m s}^{-1}$, is observationally examined and compared to theories and the preceding results of laboratory experiments. In the near wake, recirculation occurs with a relative vorticity of $\zeta \sim 20f$ (where f is the planetary vorticity) and subsequently sheds at a combination of periods resulting from the tidal oscillations and the intrinsic time scale of eddy evolution. The tidal oscillations are the predominant processes. Our analysis suggests that an island positioned in the Kuroshio with periodic and cross-stream tidal excursions is analogous to a cross-stream oscillating cylinder. Consequently, the shedding period of the vortex is synchronized to a tidal period occurring close to the intrinsic period. The free shear layer, which is characterized by an $\sim 30f$ relative vorticity band (2 km wide) and a wavy thermal front, develops between the Kuroshio and recirculation. The frontal wave occurring over a time period of 0.5–2 h resembles Kelvin–Helmholtz instability corresponding to high Re values. For the far wake, repeated cross-wake surveys suggest that cyclonic and anticyclonic vortices are alternatively present at a period close to the period of M_2 tides in agreement with near-wake measurements. Repeated along-wake surveys reveal a cyclonic eddy shedding downstream at a speed of 0.35 m s^{-1} , $1/3$ of the upstream current speed, from the near wake. In comparing our observations with the results of previous water tank experiments, an Re value of $O(10^3)$ for the submesoscale wake regime is expected.

1. Introduction

Oceanic island wakes have been extensively researched because of their significant role in the energy cascade from the large-scale flows to the small-scale turbulent dissipation and mixing (Barkley 1972; Farmer et al. 2002; Hasegawa et al. 2004; Chang et al. 2013) and due to their critical influence on surrounding biological environments (Doty and Oguri 1956; Heywood et al. 1990; Hasegawa et al. 2009). Within this context, the dynamics of oceanic wake flows on the lee side of an island are derived from theoretical and experimental investigations of circular cylinder wakes observed in laboratory tanks and from numerical simulations conducted with a steady and uniform upstream velocity

value U (Figs. 1a,b), forming a crucial Reynolds number, $Re = UD/\nu$, where D and ν are respectively the cylinder diameter and kinematic viscosity. The flow passing a cylinder at a fully developed stage is characterized by three physical features: the wake flow, the free shear layer resulting from flow separation, and the boundary layer at the front body surface, all of which evolve depending on the Re regime involved (Williamson 1996a). When $Re < 49$, the wake flow manifests as a pair of steady recirculation flows attached to the cylinder whose streamwise (along-stream) length increases with Re. In the laminar vortex shedding regime ($49 \leq Re \leq 194$), wake flow instability (Provansal et al. 1987) develops close to the recirculation tail, leading to alternating shedding of 2D vortices in the near wake, consequently forming a von Kármán vortex street in the far wake (Fig. 1a). The vortex street consists of a train of alternating positive (right row) and negative primary vortices (left row)

Corresponding author: Ming-Huei Chang, minghueichang@ntu.edu.tw

DOI: 10.1175/JPO-D-19-0035.1

© 2019 American Meteorological Society. For information regarding reuse of this content and general copyright information, consult the [AMS Copyright Policy](#) (www.ametsoc.org/PUBSReuseLicenses).

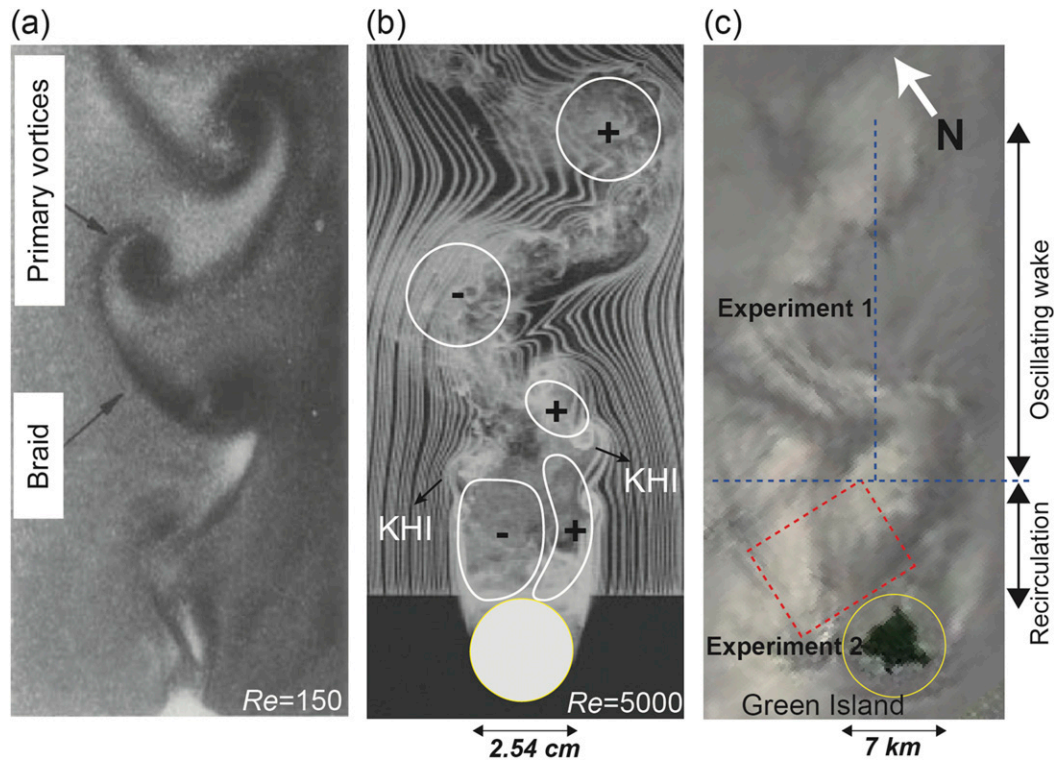


FIG. 1. Flow visualization of cylinder wakes in a water tank at (a) $Re = 150$ (Williamson 1996a) and (b) $Re = 5000$ (Prasad and Williamson 1997) and (c) MODIS snapshot image taken at 0505 UTC 9 Aug 2003 capturing wake-induced sea surface changes at a 250-m resolution. The positive and negative signs enclosed by white curves in (b) express cyclonic and anticyclonic vorticity, respectively. Kelvin–Helmholtz instabilities are denoted as KHI. The cross- and along-wake surveys conducted in Experiment 1 are indicated as blue dashed lines in (c). The red dashed box in (c) shows the region of quasi-synoptic recirculation mapping used for Experiment 2. The double-headed arrows shown in (b) and (c) respectively denote cylinder (2.54 cm) and Green Island (7 km) diameters.

connected with braids in between (Fig. 1a). The vorticity field becomes more complex when evolution enters the 3D wake transition regime ($190 \leq Re \leq 260$). Primary vortices and braids accompany two spanwise (cross-stream) propagating instabilities with streamwise vorticity respectively referred to as mode A and mode B instabilities [refer to Fig. 8 in Williamson (1996b) for further details]. The streamwise vortices are persistent even at much higher Re values. As suggested by Prasad and Williamson (1997), the shear-layer transition regime measured at $Re > 1200$ marks the onset of horizontal Kelvin–Helmholtz (KH) instability within the free shear layer (Fig. 1b), leading to shear layer rollup into coherent vorticity. An extremely high Re value ($\sim 200\,000$) spurs a transition in the boundary layer.

The period of wake evolution (or eddy shedding) T is related to the Strouhal number $St = D/UT$ with dependence on Re . Therefore, the relationship between Re and St plays a central role in determining wake patterns and evolution, which are well formulated by

$$St = 0.273 - 1.11Re^{-1/2} + 0.482Re^{-1}, \quad (1)$$

as proposed in Williamson and Brown (1998) (black curve in Fig. 2c). The St – Re diagram suggests that St increases with Re . At a constant cylinder diameter, a stronger upstream flow leads to a shorter shedding period at the same Re (Fig. 2d). The Re – St relationship (Fig. 2c) summarized from numerical island wake simulations given in Teague et al. (2005) (red triangle in Fig. 2), Huang et al. (2014) (yellow diamonds), Coutis and Middleton (1999) (green squares), Dong et al. (2007) (blue circle), and Liu and Chang (2018) (yellow star) agree well with Williamson and Brown’s empirical curve.

Questions remain regarding the capacities of classic theorems like those described above for oceanic wakes and especially when applied to field observations. First, the kinematic viscosity ν of Re must be replaced with horizontal eddy viscosity ν_h , which varies from 10^2 to $10^5 \text{ m}^2 \text{ s}^{-1}$ in the open ocean (Apel 1987). Unfortunately, a simple and robust method for measuring ν_h has not been developed. Second, it is difficult to carry out field

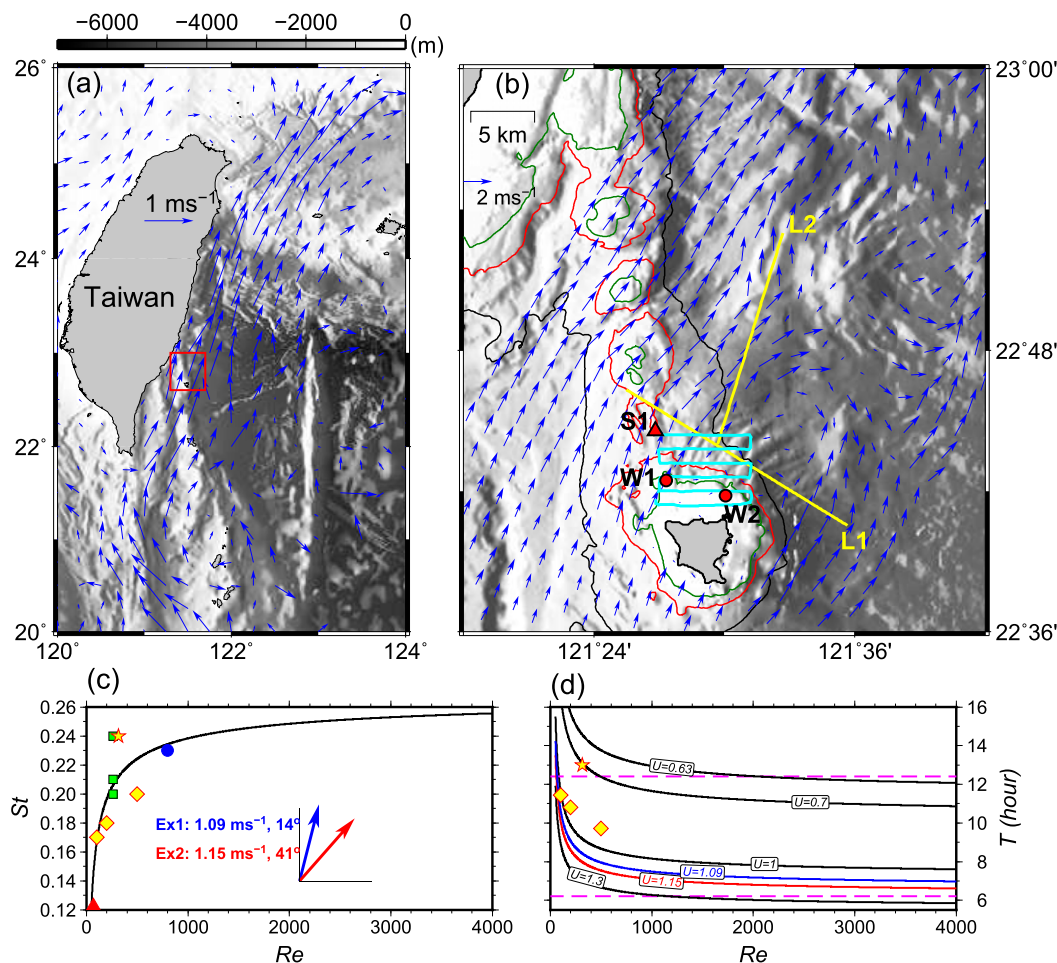


FIG. 2. (a) Bathymetry and horizontal current vectors around Taiwan measured at a depth of 30 m and at $1/4^\circ \times 1/4^\circ$ averaged from historical ship-based ADCP data. (b) Specific bathymetry within the red box in (a) with yellow lines denoting cross-wake (L1) and along-wake (L2) surveys conducted in Experiment 1, with the cyan line showing patterns of current and temperature mapping collected through Experiment 2, with red circles showing the positions of mooring W1 (left) and W2 (right) and with the red triangle showing the positioning of mooring S1. (c) The Re - St diagram formulated by $St = 0.273 - 1.113Re^{-1/2} + 0.482Re^{-1}$ (Williamson and Brown 1998) superposed with the numerical results given by Teague et al. (2005) (red triangle), Huang et al. (2014) (yellow diamonds), Coutis and Middleton (1999) (green squares), Dong et al. (2007) (blue circle), and Liu and Chang (2018) (yellow star). (d) Re - T diagram derived from (c) with $U = 0.63, 0.7, 1, 1.09, 1.15,$ and 1.3 and $D = 7$ km superposed with the numerical results of Huang et al. (2014) (yellow diamonds) and Liu and Chang (2018) (yellow star). The black, red, and green curves shown in (b) respectively represent the 1000-, 500-, and 250-m isobaths. The blue and red arrows shown in (c) respectively denote upstream velocity U values measured during Experiments 1 and 2. The dashed magenta lines shown in (d) denote the M_2 and M_4 tidal periods.

measurements to simultaneously reach sufficient temporal and spatial resolutions to measure wake evolution. As a result, observations are mostly composed of quasi-synoptic “snapshots,” for example, Coutis and Middleton (1999), Heywood et al. (1996), Hasegawa et al. (2004), Chang et al. (2013), and Neill and Elliott (2004). Third, a “steady” free stream is rarely found in the ocean. Black and Gay (1987) and Signell and Geyer (1991) noted that the periodic incoming flow plays an important role in wake generation and in the period of vortex shedding

referring to the effect of “phase eddies.” Moored current meter observations made from the lee side of the Bass Point (a 4-km-long headland off the Australian coastline) reveal that recirculation on lee side occurs at the diurnal frequency, which relates to diurnal tides (Denniss et al. 1995). In combining observations with numerical experiments, Denniss et al. (1995) noted that “the size and frequency of eddy shedding in the lee of the headland depended on the degree of variability of the inflowing free stream, with a diurnal component in

the free stream appearing to cause the oscillations in the wake of diurnal frequency.” As ocean currents are normally variable, the findings given by Black and Gay (1987) and Denniss et al. (1995) are relevant to oceanic island wakes but appear to have attracted less attention. Furthermore, Earth’s rotation and stratification must be considered. The inertial instabilities (in Northern Hemisphere) favor the survival of cyclonic eddies and destabilizes or breaks anticyclonic eddies, which could adapt the vortex street features (e.g., Caldeira and Sangrà 2012; Dong et al. 2007; Molemaker et al. 2015; Perfect et al. 2018). Finally, vorticity generation does not simply involve horizontal eddy viscosity control, that is, bottom friction may also play an important role in shallow water wakes (Wolanski and Hamner 1988).

Of particular interest is the evolution of the wake flow that occurs when the strong Kuroshio passes a small island (Figs. 2a,b). The Kuroshio, which is the western boundary current of the subtropical western North Pacific Ocean, curves through the Luzon Strait and flows north along the east coast of Taiwan. Despite the strong impact of impinging eddies on its velocity structure and transport (Jan et al. 2017; Chang et al. 2018), it is roughly 100–150 km wide and maintains a typical flow speed of 1–1.5 m s⁻¹ on average (Fig. 2a). The presence of numerous small islands along the Kuroshio’s path forms complex wakes with submesoscale eddies, for example, Babuyang and Batan Island wakes in the Luzon Strait (Zheng et al. 2008), the Green Island wake east of Taiwan (Chang et al. 2013), and the Aoga-shima Island wake off the coast of Japan (Hasegawa et al. 2004). Green Island is situated at the Kuroshio’s main axis (Figs. 2a,b), creating an opportunity to observe how a strong current interacts with the small island (Chang et al. 2013) and with the abrupt bathymetry adjacent to the island (Chang et al. 2016).

Previous numerical simulations of island wakes present a value of $Re \sim O(10^2)$ (Fig. 2c). However, a well-defined vortex street consisting of a clear train of alternating positive and negative vortices at lower Re values as shown in Fig. 1a is rarely found in satellite images (e.g., Chang et al. 2013; Hsu et al. 2017). It could be partly due to the occurrences of inertial instability tending to destabilize the anticyclonic eddies, which could adapt the vortex street features. On the other hand, surface signatures of the Green Island wake shown in Fig. 1c are surprisingly consistent with the wake signatures, which are characterized by an elongated recirculation pair at the near wake and a wavy tail at the far wake according to water tank experiments conducted at $Re = 5000$ (Fig. 1b). As indicated by the positive and negative signs and the double arrows shown in Fig. 1b, surface signatures reflect a pair of cyclonic and anticyclonic eddies in

the near field and an oscillating wake in the far field due to eddy shedding. We expect to find a similar situation from a MODIS image of the Green Island wake (Fig. 1c). Kelvin–Helmholtz billows can be observed from the free shear layer according to water tank experiments, but they are absent from satellite images of the Green Island wake, presumably due to the insufficient resolution of satellite images. We perform two observational experiments to investigate island wake behavior and to examine vortex evolution in the context of classic theorem and water tank experiments.

2. Data and experiments

Our experiments examine the oscillating wake through along- and cross-wake surveys (blue dashed lines in Fig. 1c) and map anticyclonic recirculation in the near wake (red dashed boxes in Fig. 1c). Therefore, two experiments were performed on two trips aboard Taiwanese R/V *Ocean Researcher III (OR3)* to observe wake evolution. Experiment 1 (Ex1) was conducted in September 2013 to investigate far wake evolution. Synoptic snapshots of currents and hydrographical data such as those captured through satellite remote sensing or from the results of numerical models could not be obtained through in situ observation due to rapid patterns of wake flow evolution. As a result, the experiment did not emphasize 3D spatial mapping. Instead, repeated 12 cross-wake and 4 along-wake surveys (yellow lines in Fig. 2b) of the lee side of Green Island were conducted during Ex1 to respectively capture cross- and along-wake variations as a function of time. The cross-wake track (marked as L1 in Fig. 2b) was designated ~9 km downstream from Green Island, where the shedding eddy can fully develop. The along-wake track (marked as L2 in Fig. 2b), with its southern end connected to the cross-wake track, was oriented almost parallel to the main axis of the Kuroshio according to the current’s upstream direction 14° to the north (blue arrow shown in the inset of Fig. 2c). An estimate of the upstream current velocity is provided below. Individual surveys respectively took ~2 and ~1.5 h to perform in cross-wake and along-wake transects. In total, cross- and along-wake measurements were respectively performed for ~25 and 6 h. Current and hydrographic data were respectively collected along survey lines via ship-based ADCP (acoustic Doppler current profiler) and tow-yo Underway CTD (UCTD).

Experiment 2 (Ex2) was conducted in July 2014. Field observations focused on the region of anticyclonic recirculation to the north of and on the immediate lee side of Green Island (Fig. 2b). Ten quasi-synoptic snapshots of currents and surface hydrographic data were obtained through rapid surveys [~ 8 kt (1 kt ≈ 0.51 m s⁻¹)]

conducted along the cyan line shown in Fig. 2b using ship-based ADCP and surface CTD, respectively, covering a region of $7 \text{ km} \times 5 \text{ km}$. We expected quasi-synoptic snapshots to not be significantly distorted (e.g., Chang et al. 2013), as each survey took $\sim 3 \text{ h}$ to perform, which should be considerably shorter than the time period of wake variability. Transects sliced through the near wake at an interval of roughly 1 km . The ship-based ADCP and surface CTD sampled at an interval of 1 min yielding an along-track resolution of 240 m . The spatiotemporal sampling of ship-based ADCP and surface CTD data was linearly interpolated to $0.5 \text{ km} \times 0.5 \text{ km}$. Three ADCP moorings were used to supplement Ex2. Two of the ADCP moorings, W1 and W2, were respectively deployed close to the western edge of the wake and within the wake and were positioned within the area covered by ship-based surveys of anticyclonic recirculation (red dots in Fig. 2b). W1 and W2 respectively measured current velocities of $30\text{--}150 \text{ m}$ and $10\text{--}70 \text{ m}$ for two months (14 July–12 September 2014) covering Ex2 ship-based surveys. The sampling interval was set to 5 min . In addition, an ADCP mooring S1 was deployed outside of the wake region (red triangle in Fig. 2b) to measure the current velocity in $40\text{--}480 \text{ m}$ with a sampling rate of 2 min and was used to identify the background tidal motion. The S1 measurement period ran from May 2011 to October 2011, $\sim 3 \text{ years}$ from the timing of the above observations.

Upstream velocities U measured during the two experiments were determined by taking the averaged velocity from the upper 100 m upstream of Green Island measured immediately before the downstream surveys. During Ex1, the upstream velocity magnitude was measured as 1.09 m s^{-1} and was directed 14° to the north (blue arrow shown in the inset of Fig. 2c). During Ex2, the magnitude of the upstream velocity was measured as 1.15 m s^{-1} , slightly exceeding the value measured during Ex1, but the current was directed 41° to the north (red arrow shown in the inset of Fig. 2c) and significantly inclined to the east.

3. Results

a. Recirculation

The Ex2 surveys were intended to construct a basic account of the observed wake flow pattern and of its evolution in the immediate wake. These surveys were simultaneously supplemented with moorings W1 and W2 to respectively measure current velocities at the western edge of anticyclonic recirculation and within the recirculation area (red circles in Fig. 2b). Ten continuous quasi-synoptic snapshots of current velocities measured at 16.5 m and of sea surface temperatures show significant

variations in flow and temperature patterns within the recirculation area. Ship surveys were performed from the northwestern to southwestern corners of the surveyed area along the path shown in Fig. 3 (red line at stage 1). The starting time t of each quasi-synoptic mapping period (when the ship was positioned at the northwesternmost point) is denoted in the top-left corner of each panel. Two successive surveys conducted from the same location typically last over $\sim 3.1 \text{ h}$. The loss of synopticity observed may be of an acceptable level since wake evolution occurred over ~ 12 or $\sim 6 \text{ h}$ as discussed below.

In stage 1 ($t = 0$), the flow in the wake is clearly identified as the northward current ($\sim 1.5 \text{ m s}^{-1}$) associated with the Kuroshio on the western side of the survey area and is a much weaker current ($0.2\text{--}0.5 \text{ m s}^{-1}$) without obvious patterns present in the rest of the area. Remarkable discrepancies of flow patterns from stage 1 appear in the second stage ($t = 3.17 \text{ h}$), showing that the Kuroshio, which is identified by higher surface temperatures and stronger current vectors, occupies $>50\%$ of the survey area as a result of the current's eastward curving. The strong curved flow is persistent from stage 2 ($t = 3.17 \text{ h}$) to stage 4 ($t = 9.58 \text{ h}$) and eventually forms anticyclonic recirculation, which is most distinct in stage 4. Subsequently, this anticyclonic recirculation seems to gradually propagate northward from stage 5 ($t = 12.75 \text{ h}$) to stage 7 ($t = 18.92 \text{ h}$). In stage 7, cyclonic circulation likely related to recirculation forming along the island's eastern boundary occupies the southeastern part of our survey area while anticyclonic recirculation maintains its northward propagation. Hereafter, evolution from stages 8–10 is unexpectedly rapid, that is, anticyclonic recirculation forms again (stage 8) and propagates northward (stage 9), which is immediately followed by the presence of another pattern of anticyclonic recirculation within 3 h (stage 10). Similarly, cyclonic circulation associated with recirculation from the island's eastern edge is found the region previously free of the northward propagating anticyclone. As reported above, the specific period of wake flow evolution is not recognizable due to an insufficient temporal resolution. However, the evolutionary pattern occurs over a longer period and over two shorter periods of roughly $t = 0\text{--}15.83 \text{ h}$ and $t = 18.92\text{--}28.5 \text{ h}$, respectively. Notably, in stages 1–9, a wave-like (or serrated) structure appears at the front between the Kuroshio and wake water depicted by a 30°C isotherm (white curves in Fig. 3) and is largely collocated with the strong horizontal shear layer.

From simultaneously moored observations collected at W1 and W2, the time series (Fig. 4) reveals not only the flow evolution revealed in quasi-synoptic snapshots but also the period of wake flow evolution and sea surface temperature variation related to alongfront waves.

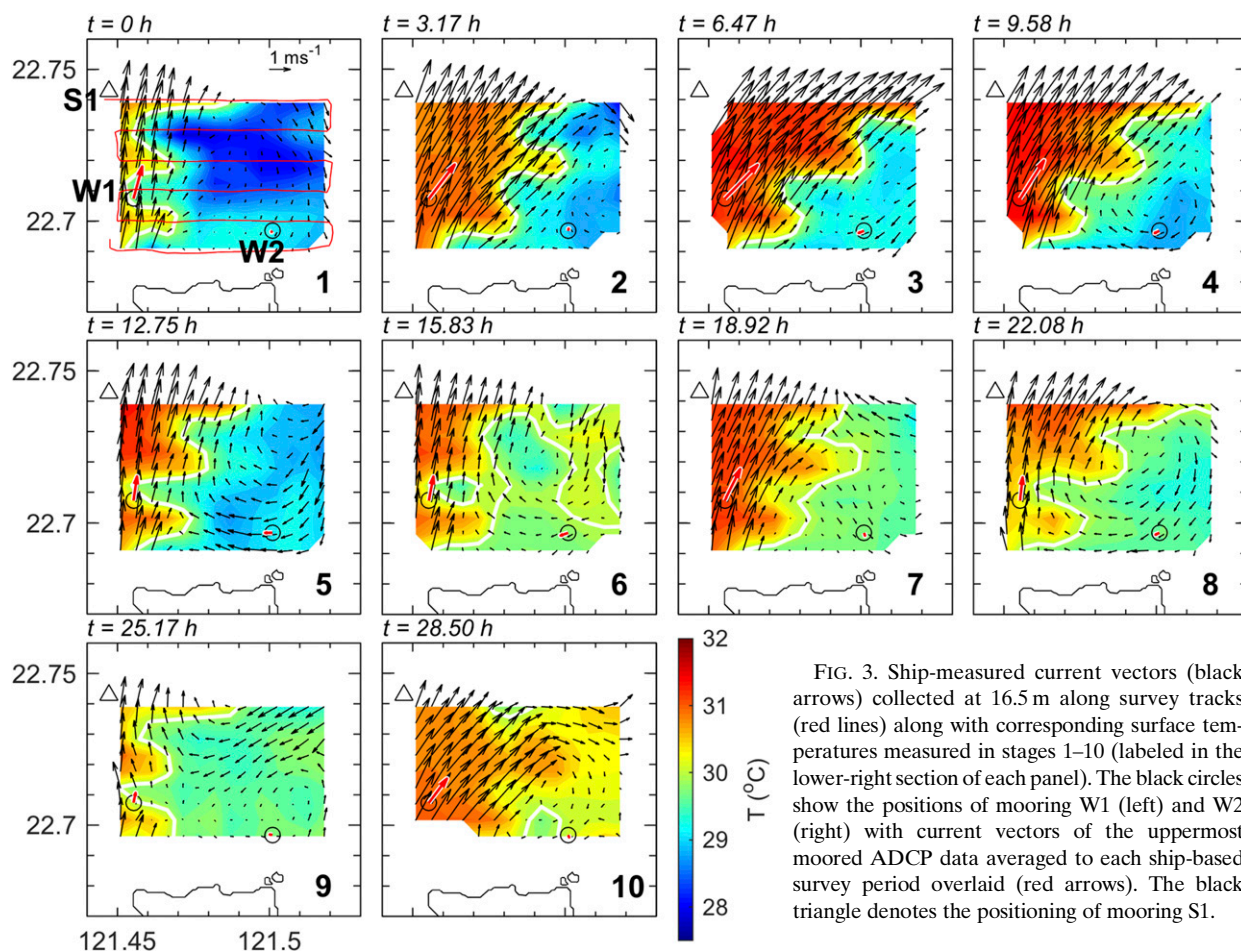


FIG. 3. Ship-measured current vectors (black arrows) collected at 16.5 m along survey tracks (red lines) along with corresponding surface temperatures measured in stages 1–10 (labeled in the lower-right section of each panel). The black circles show the positions of mooring W1 (left) and W2 (right) with current vectors of the uppermost moored ADCP data averaged to each ship-based survey period overlaid (red arrows). The black triangle denotes the positioning of mooring S1.

First, the ship-measured velocities are compared to the moored velocity measurements. The measurement depth range at mooring W1 is strongly influenced by the vertical displacement of ADCP floating induced by energetic currents. The depth of the uppermost measurement varies from 30 to 100 m as shown in Fig. 4a. Current vectors averaged from the uppermost moored ADCP data for each ship-based survey period are overlain (red arrows in Fig. 3) with the vectors measured from the ship. Not surprisingly, the moored current velocities and those measured from the ship coincide very well across the 10 surveys. Second, in linking the moored observations to depictions of wake evolution (Fig. 3), we identify 1) a stronger pattern of positive (eastward) velocity at W1 that reflects the Kuroshio curving into the wake area; 2) the stronger negative (westward) velocity level measured at W2 denotes the formation of anticyclonic recirculation in response to the returned flow of Kuroshio curving; and 3) the positive (eastward) velocity measured at W2 may be associated with the incursion of cyclonic

recirculation emitted from the island's eastern boundary, for example, stages 7 and 9 in Fig. 3. Along this line of reasoning, Fig. 4a shows that the zonal velocity at W1 increased from 0000 to 1100 UTC on 15 July, which corresponds to stages 2–4 in Fig. 3. This period is recognized as the first instance of Kuroshio curving (KC) and is denoted as KC1. Corresponding anticyclonic recirculation (AR) patterns identified at W2 are marked as AR1 (Fig. 4b) and lag behind KC1 by 1–4 h. The second KC event (marked as KC2) lasts over a shorter period running from 1600 to 2100 UTC on 15 July (stage 7–8) and corresponds to anticyclonic recirculation (AR2) at a similar time scale. The third KC–AR pair is denoted as KC3 and AR3 in Fig. 4. Note that only a small segment of the KC3–AR3 event (stage 10) occurs during the period of ship measurement. Therefore, our interpretation and analysis of the KC1–AR1 and KC2–AR2 events is emphasized. Kuroshio curving events are often followed by a relaxation period, revealing a weak westward velocity as denoted as R1 and R2 in Fig. 4a. R1 and R2 roughly occur within stages 5–6 and stages 8–9, respectively,

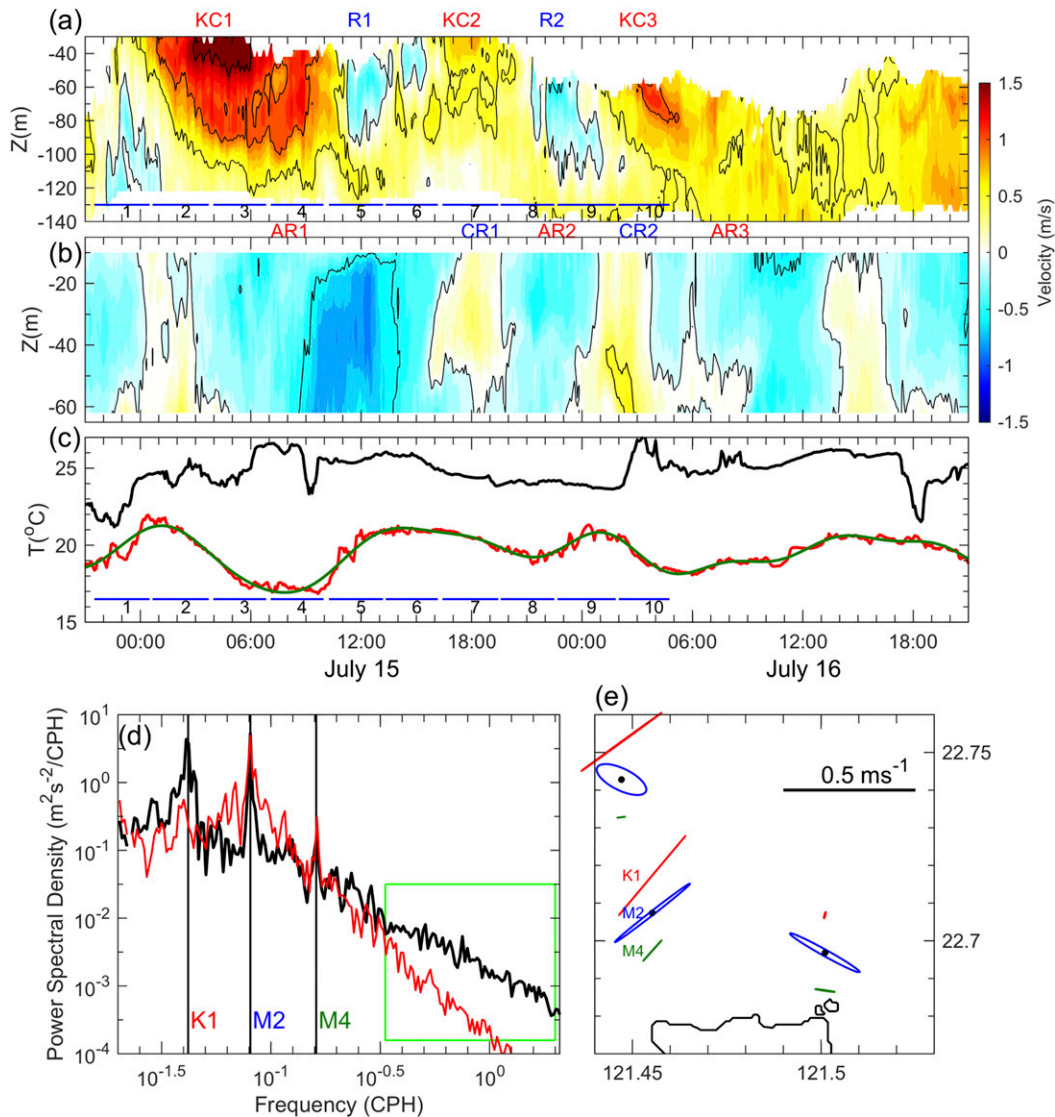


FIG. 4. Contour plots of zonal velocity at (a) W1 and (b) W2. (c) Temperature time series at W1 (130 m; red curve) superposed with 1-h low-pass-filtered data (green curve) and with W2 (70 m; black curve). (d) Spectra of zonal velocity averaged to 60–100 m at W1 (black curve) and zonal velocity averaged to 20–60 m at W2 (red curve). (e) Tidal ellipses of K_1 (red), M_2 (blue), and M_4 (green) observed at W1 (bottom left), W2 (right), and S1 (top left). Black dots denote mooring locations collocated with the center of the M_2 tidal ellipse. Blue lines shown in (a) and (c) denote the period of each ship-based survey. Vertical lines in (d) denote spectral peaks measured at 4.18×10^{-2} , 8.05×10^{-2} , and 1.61×10^{-1} cph corresponding to K_1 (23.92 h), M_2 (12.42 h), and M_4 (6.21 h) tidal constituents, respectively. The spectral bump shown over 0.5–3 h is denoted by the green box.

showing that the ARs propagate northward. During this phase, the Kuroshio flows northward or slightly northwestward as in stage 1. Kuroshio curving and subsequent relaxation form a complete cycle of zonal velocity variation repeatedly occurring in over 2-month moored measurement period from W1. In contrast, AR events are often followed by cyclonic recirculation (CR) appearing in the southeastern section of our survey area after AR propagates northward as described above.

CR events drive the eastward current velocity measured at W2 as shown with stages 7 and 9 in Fig. 3 and are denoted as CR1 and CR2 in Fig. 4b. Likewise, the AR–CR pair forms a complete cycle of zonal velocity variation that is repeatedly observed from our 2-month moored measurements drawn from W2. A spectral analysis of the entire time series of zonal velocity measured at W1 and W2 is used to clarify the time periods of wake variations. A spectral analysis of zonal velocities averaged

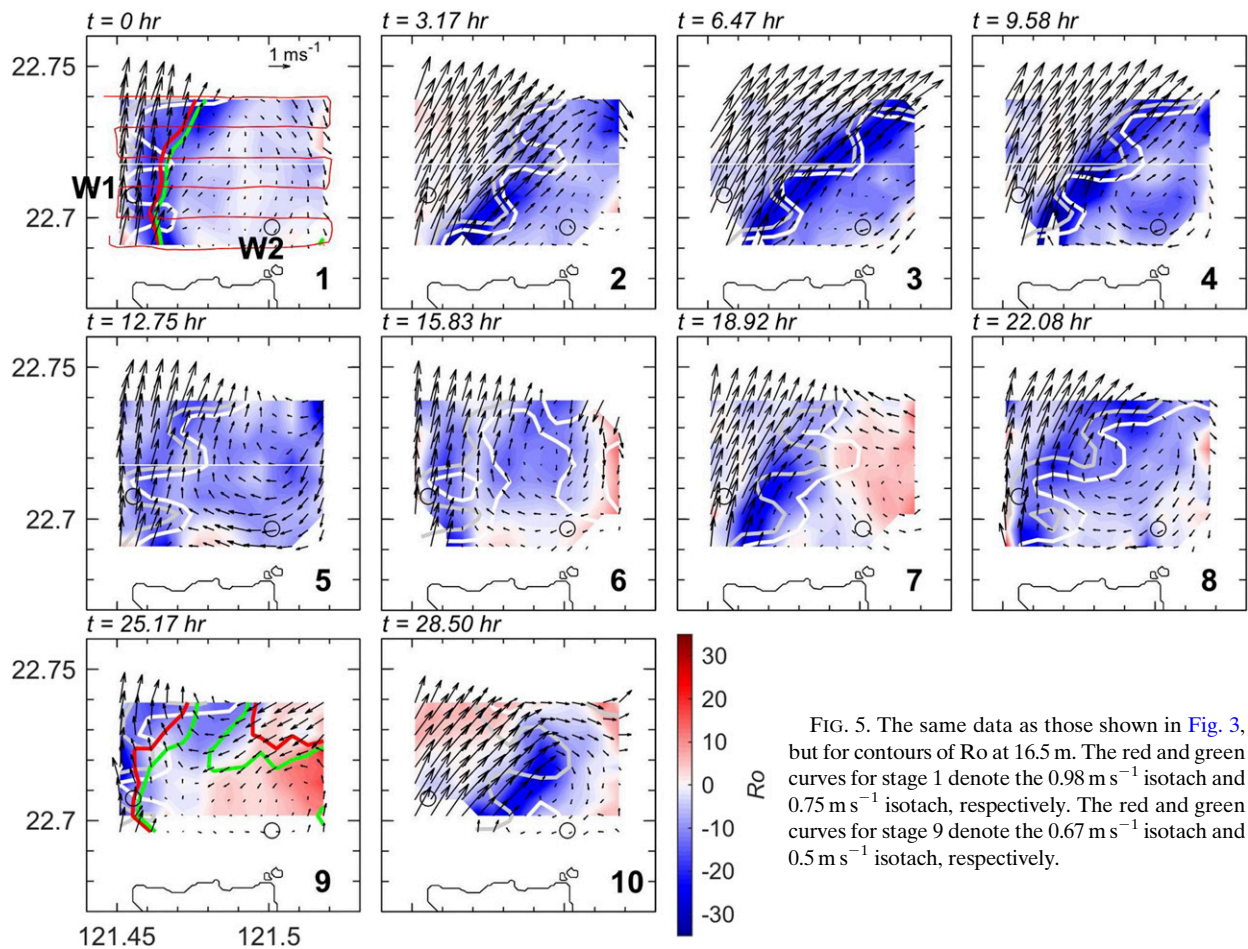


FIG. 5. The same data as those shown in Fig. 3, but for contours of Ro at 16.5 m. The red and green curves for stage 1 denote the 0.98 m s^{-1} isotach and 0.75 m s^{-1} isotach, respectively. The red and green curves for stage 9 denote the 0.67 m s^{-1} isotach and 0.5 m s^{-1} isotach, respectively.

at 60–100 m from W1 (black curve in Fig. 4d) reveals spectral peaks at 4.18×10^{-2} , 8.05×10^{-2} , and 1.61×10^{-1} cph corresponding to the K_1 (23.92 h), M_2 (12.42 h), and M_4 (6.21 h) tidal constituents, respectively. However, only the M_2 and M_4 signals stand out when applying a spectral analysis of average zonal velocity levels of 20–60 m at W2 (red curve in Fig. 4d). Thus, the KC1–R1 cycle observed at W1 and the AR1–CR1 cycle are likely related to the M_2 tide. The KC2–R2 cycle observed at W1 and the AR2–CR2 cycle are likely related to the M_4 tide as well. The role of the M_2 and M_4 tides in the formation of the wake vortex are elaborated on further in section 4.

b. Free shear layer

Except in stage 10, the sea surface temperatures shown in Fig. 3 also present a wave-like (or serrated) structure with three crests and three troughs that appears at the front between warm water from the Kuroshio and cold wake water approximately separated by 30°C isotherms (white curves in Fig. 3). To further examine the frontal structure, the Rossby number (Ro) based the ratio between relative

vorticity ξ , where $\xi = \partial_x v - \partial_y u$, and planetary vorticity f is computed and shown in Fig. 5. We find that $|Ro|$ within the recirculation area is typically valued at ~ 10 – 20 , suggesting that the relative vorticity value is 10 times higher than the planetary vorticity value in agreement with previous observations (Chang et al. 2013) and numerical modeling results (Liu and Chang 2018). Elsewhere, the most noticeable feature is a band of even stronger Ro values ranging from 20 to 30 presumably originating at the island’s lateral boundaries and shifting laterally through changes in recirculation. This band of strong Ro values is called a “free shear layer” (FSL) as defined in previous related works involving water tank experiments (e.g., Prasad and Williamson 1997). FSLs have a width of ~ 2 km and mostly collocate with frontal structures characterized by isotherms of 30°C (white curves) and 30.5°C (gray curves). The isotherms appear as wavy (or zigzag) shapes locked with the FSL, and we find no distinct signs of along-shear propagation from our nine surveys (stage 1–9).

The distance–depth contours of the Ro characterizing the FSL along a cross-wake transect (white horizontal

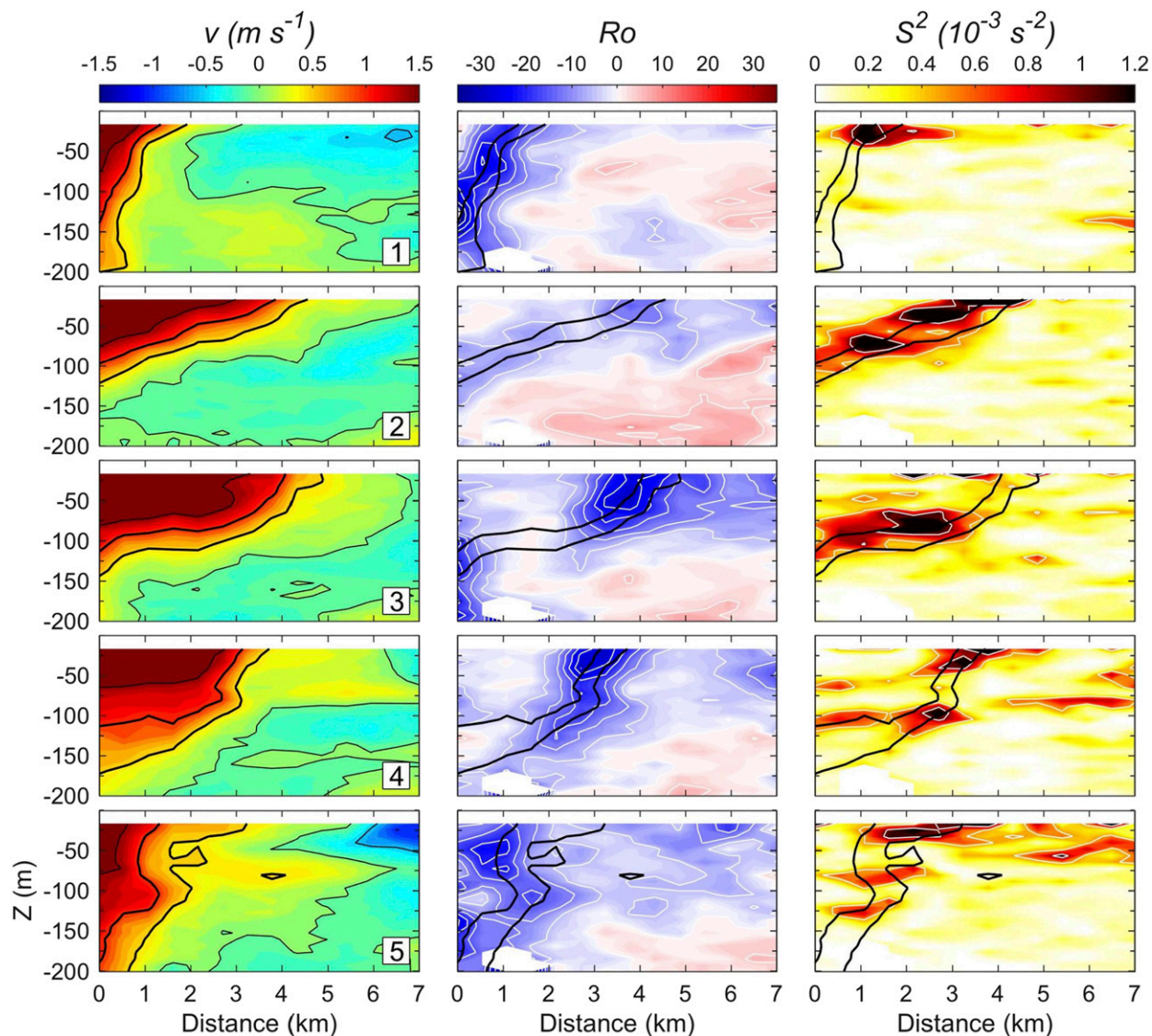


FIG. 6. Distance–depth contours of (left) meridional velocity, (center) Ro , and (right) vertical shear squared S^2 values measured along a cross-wake transect shown as white horizontal lines in Fig. 5 for stages 1–5 (labeled in the lower-right section of each panel in the left column). The black curves shown in meridional velocity contours reflect isotachs of $-0.5, 0, 0.5, 1, \text{ and } 1.5 \text{ m s}^{-1}$. The black curves shown in Ro and S^2 contours reflect isotachs of 0.5 and 1 m s^{-1} .

lines in Fig. 5) reveal the tilting of FSL in the vertical direction (panels in the second column of Fig. 6; stages 1–5). This tilting is clearly related to the vertical structure of the Kuroshio’s core curving toward the island’s leeward side in a vertically asymmetric manner (the first column). As a result, the 0.5 and 1 m s^{-1} isotachs collocate well with the FSL. The vertical shear squared, $S^2 = (\partial_z u)^2 + (\partial_z v)^2$, is examined, as well. We found that the more the isotachs tilt, the weaker the Ro in the FSL becomes, but the opposite is true for S^2 (the third column). The tilting of the isotach immediately enhances vertical shearing and (potentially) turbulence mixing

when the threshold for vertical shear instability is reached consistent with Chang et al. (2013) and Liu and Chang (2018).

c. Oscillating wake

The upstream current magnitude observed from the far wake experiment is measured as 1.09 m s^{-1} , which is nearly identical to that observed from the previous near wake experiment, but the current direction shifts from 41° to 14°N (Fig. 2c). This implies a similar dynamic regime of wake evolution with a different region for eddy formation on the leeward side. The 12 repeated

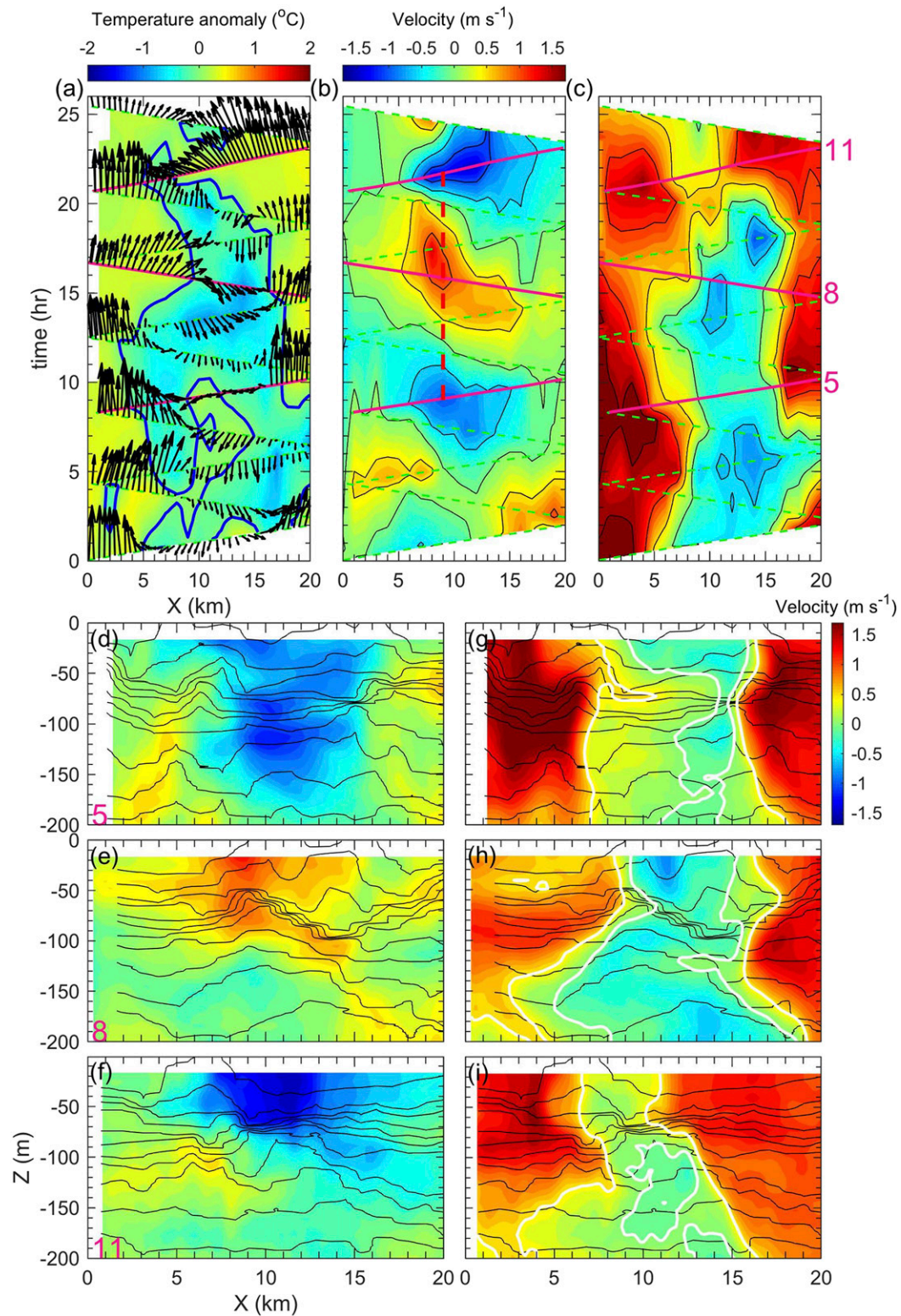


FIG. 7. Cross-wake distance–time contours of (a) temperature anomalies with corresponding current, (b) cross-stream, and (c) along-stream velocities measured at 20 m. Distance–depth contours of cross-stream velocity taken from surveys (d) 5, (e) 8, and (f) 11 and of along-stream velocity taken from surveys (g) 5, (h) 8, and (i) 11. The magenta lines shown in (a)–(c) show patterns identified from surveys 5, 8, and 11 overlain on

surveys conducted along the L1 section (Fig. 2b) show rapid variations in current velocity and hydrography (Figs. 7a–c) related to the passage of an eddy shedding from the near wake. Here, the flow field is expressed as the cross-stream velocity u_r and along-stream velocity v_r obtained by rotating the coordinate system 14° (upstream current direction) clockwise. Isotherm doming up to 50 m primarily occurs in the upper 70 m for all of the surveys. Either one or two cold domes associated with submesoscale eddies were captured in each survey. Here, surveys 5 (Figs. 7d,g), 8 (Figs. 7e,h), and 11 (Figs. 7f,i) are used to further illustrate the vertical structures of current and isotherms along the L1 transect. During survey 5, the isotherms present two cold domes with their centers separated by ~ 10 km. Each center is roughly collocated with the 0.5 m s^{-1} isotach of the along-stream velocity at the eastern and western flanks, respectively (Fig. 7g). In survey 8, the measured cold dome pair draws closer with centers separated by ~ 5 km and likely to merge (Fig. 7h). As a result, the region formed by the 0.5 m s^{-1} isotach of along-stream velocity is scaled down slightly and becomes vertically asymmetric. During survey 11, only one cold dome was detected (Fig. 7i) and the region formed by the 0.5 m s^{-1} isotach of along-stream velocity was scaled down to half that used for survey 5. A full account of the observed patterns of wake evolution is summarized as a distance–time plot of temperature anomalies at 22 m and as current vectors at 16 m in Fig. 7a. Isotherm doming is characterized by a negative temperature anomaly (enclosed by the blue curve). Over 0–9 h (surveys 1–5), two distinct bands of negative temperature anomalies form the cold dome pair as shown in Fig. 7g. After 10–16 h (surveys 6–8), the wide range of negative temperature anomalies reflects a shorter distance between the cold domes as shown in Fig. 7h. The remaining measurements (17–26 h; surveys 9–12) show a single cold dome (Fig. 7i). Consistent with the temperature anomaly observed, the current vectors (u_r , v_r) reveal curved and returned currents in response to the passage of eddies. Periodic variations associated with the wake are not easily recognized from the current vectors (Fig. 7a) but become evident when contouring individual cross-stream velocity (Fig. 7b) and along-stream velocity (Fig. 7c). Positive and negative u_r values alternate, accompanied by a wavy pattern of returned flows of v_r enclosed by the 0 and 0.5 m s^{-1} isotachs.

The leftward and rightward currents respectively correspond to leftward and rightward swinging returned flows. Notably, strong cross-stream velocities are often limited in the upper 100 m, for example, Figs. 7e and 7f, with the exception of those observed in surveys 4 (not shown) and 5 (Fig. 7d). The period lasts ~ 13 h, as roughly estimated from the time difference between peak velocities measured from surveys 5 and 11 (dashed magenta line in Fig. 7b). The period occurs close to that of the semidiurnal tide as indicated in Ex2.

The four along-stream surveys (L2 as indicated in Fig. 2) conducted immediately following the cross-stream surveys reveal convincing signs of cyclonic and anticyclonic eddies propagating downstream (Fig. 8a), resulting in the formation of an oscillating or swinging wake as revealed from the cross-wake surveys. The point of zero velocity, representing the eddy's center, propagates 5 km downstream over 4 h (red line), suggesting a propagation speed of 0.347 m s^{-1} . Vertical profiles of cross-stream velocity and temperature derived from the first two surveys (Figs. 8b,c) show that the eddy's center characterized by isotherm doming is collocated with the point of zero velocity as was expected. The amplitude of this doming is measured as ~ 50 m and is primarily observed within the upper 70 m in agreement with that observed in the cross-stream section. Again, strong cross-stream velocities are limited to the upper 100 m (Figs. 8b–e). Another anticyclonic eddy following the previous cyclonic eddy can be identified at $Y \sim 5$ km from the fourth survey (Figs. 8a,e). In summary, the scenario depicted by the cross-wake and along-wake surveys successfully validates the presence of an oscillating tail at the far wake as shown by the water tank experiment (Fig. 1b) and satellite images (Fig. 1c) resulting from the alternating passage of cyclonic and anticyclonic eddies. As a rough estimate, the oscillation period of far wake evolution occurs close to the semidiurnal tidal period, echoing that observed for the near wake.

4. Wake period

To date, the period of vortex shedding revealed from our ship surveys from near-wake and far-wake areas shows a considerable degree of uncertainty, that is, 1) ship-based mapping (Ex2) of the near wake area reveals long (>10 h) and short periods (<10 h) of vortex evolution; 2) the repeated cross-wake transects (Ex1)

←

the results of all ship surveys (green dashed lines). The black curves shown in (d)–(i) denote isopycnals of $21\text{--}26 \text{ kg m}^{-3}$ measured at an interval of 0.5 kg m^{-3} . The white curves shown in (g)–(i) denote isotachs of 0 and 0.5 m s^{-1} .

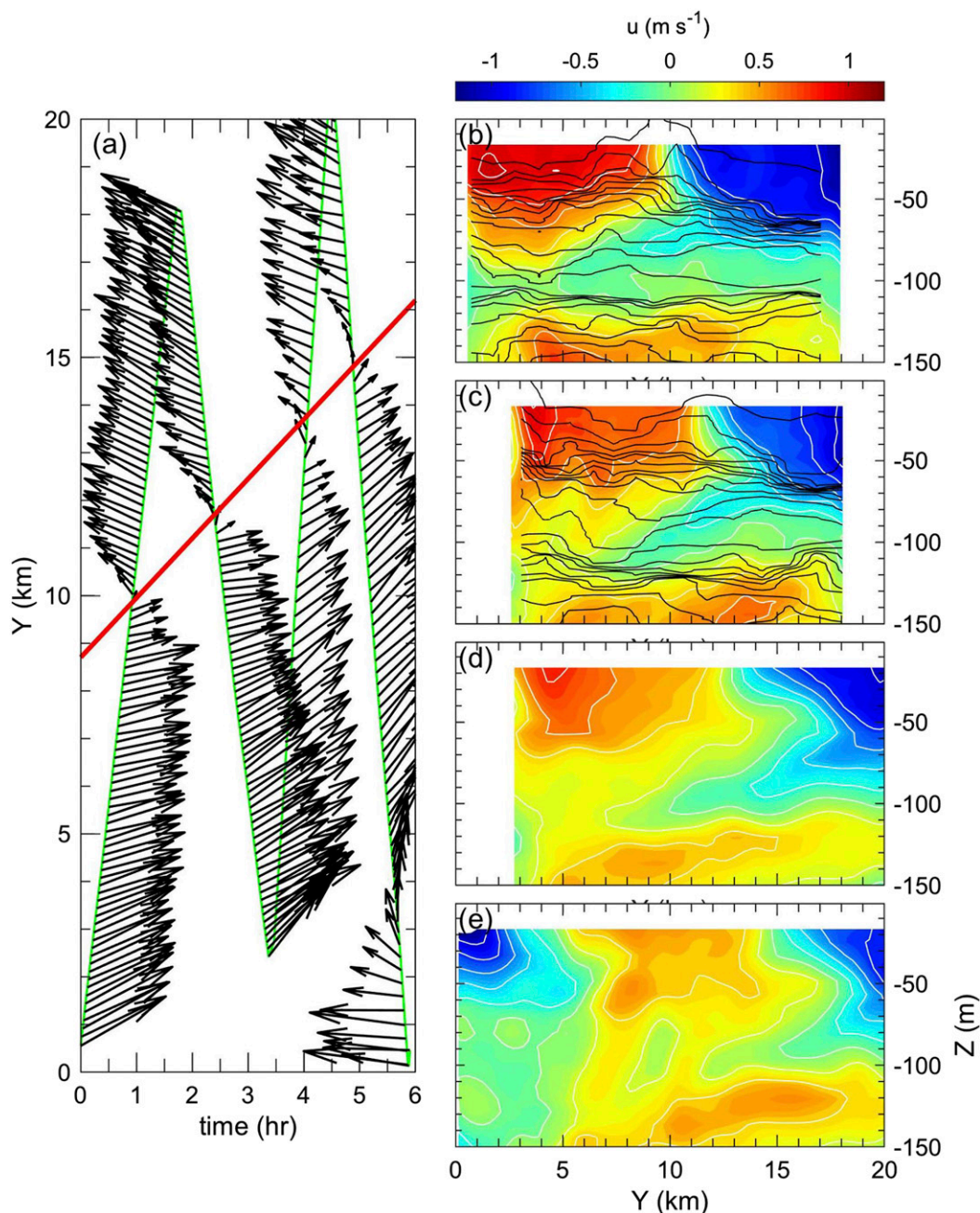


FIG. 8. (a) Time–(along-wake) distance plot of current vectors and distance–depth contours of cross-wake velocity following from (b)–(e) four surveys. The black curves shown in (b) and (c) denote isopycnals of $21\text{--}26\text{ kg m}^{-3}$ measured at an interval of 0.5 kg m^{-3} .

show wake oscillation occurring over a period of $\sim 13\text{ h}$; and 3) moored observations of zonal velocity close to the western edge of the wake and within the wake reveal significant M_2 and M_4 tidal periods (Fig. 4d). It is not clear whether the intrinsic shedding and tidal periods independently coexist, interplay or synchronize as specified in Dennis et al. (1995). To address this uncertainty, we first estimate their period of intrinsic

shedding in accordance with Strouhal number dependency. The natural period of wake motion as a function of Re is obtained using St , yielding

$$T = D/USt, \quad (2)$$

where St is substituted by the Re – St relationship in (1). Given an island diameter of $D = 7\text{ km}$ as suggested by Chang et al. (2013) for the Green Island case, the

Re– T diagram for different U values is shown in Fig. 2d, showing higher levels of upstream velocity occurring over a shorter period of wake oscillation. Numerical studies by Huang et al. (2014) (yellow diamonds; $U = 1 \text{ m s}^{-1}$) and Liu and Chang (2018) (yellow stars; $U = 0.7 \text{ m s}^{-1}$) present results that coincide with this relationship. Diagrams corresponding to the wide range of U suggest that the oscillating period of the Green Island wake ranges from 5 to 16 h for $\text{Re} > 50$. We suggest that $\text{Re} \sim O(10^3)$ for the submesoscale wake regime in the next session. If $\text{Re} \sim 1000$, the range of the oscillating period is shortened to approximately 5–12 h. Because the uncertainty of U remains, we choose the wider range of St-based period, 5–16 h, for the discussion hereafter. It is noted the above range (5–16 h) covers the tidal periods of M_2 and M_4 . Previous ship-based mapping (Fig. 3) and simultaneously moored measurements (Figs. 4a,b) indicate that the development of recirculation is characterized by 1) higher positive (eastward) velocities observed at W1 directing Kuroshio curving into the wake area and 2) a stronger negative (westward) velocity at W2 indicating the arrival of the southern part of anticyclonic recirculation in response to a returned flow of Kuroshio curving. The two events have a time lag of several hours (Figs. 4a,b and the rest of the time series of moored measurements). It is thus useful to compute the cross-spectral density between zonal velocities at W1 and W2 (Fig. 9), both of which involve a 2-month measurement period, as anticipated spectral peaks or bumps forming in an St-based period of 5–16 h in terms of cross-spectral density with a reasonable lag time may indicate the wake period.

Cross-spectral density values (Fig. 9a) present two spectral peaks in the M_2 and M_4 tidal periods (red vertical lines) within the St-based period (yellow shading). Otherwise, two bumps centered at 7.4 and 8.6 h (dashed vertical red lines) could indicate the intrinsic shedding period. However, the two bumps are insignificant, as their cross-spectral densities are not remarkably higher than those measured at adjacent frequencies in view of the 95% confidence intervals (gray shading in Fig. 9a). On the lee side of Green Island, recirculation was identified to be the most impactful process in previous studies (Chang et al. 2013; Hsu et al. 2017) and in the present study (Fig. 3). Therefore, eddy shedding proceeding with tidal frequencies is at least believed to constitute a first-order process. Statistically speaking, the cross-spectral analysis further demonstrates that zonal velocities measured at W1 present a phase lag of $-\pi/2$ at M_2 and M_4 tidal frequencies from those measured at W2 (red vertical lines in Fig. 9b). The negative phase lag values observed can be attributed to the opposing flow directions observed at the two sites. In other words, the eastward velocity

measured at W1 associated with Kuroshio curving shapes the westward velocity at W2 as a result of recirculation presenting a phase lag of quarter tidal frequency, that is, 3.1 and 1.55 h for the M_2 and M_4 tides, respectively. In general, the tidal movements do not vary considerably in terms of velocity between two sites separated by only 5 km. A recirculating flow forming in the tidal period induced by small topographic features (e.g., Signell and Geyer 1991) constitutes an exception.

Although the two bumps centered at 7.4 and 8.6 h showed in the cross-spectral density are not statistically significant, they imply the possible effective periods other than the tidal periods. To further examine the wake period as a function of time, we apply the methodology of Torrence and Compo (1998) and Grinsted et al. (2004) to compute the wavelet spectra and cross-wavelet spectra, respectively (Fig. 10). We put the focus on the range of St-based period as enclosed by two magenta lines in each panel. At the wake edge (W1), a band of high wavelet power centered to M_2 tidal period nearly persists throughout our 2-month measurements (Fig. 10a). Before 16 August, the wavelet power along this band is stronger and mostly falls within a 95% confidence level (black curves). The opposite is true for the wavelet power along the band after 16 August. It is noticed that the wavelet power around the M_4 period has only sparse and small fractions enclosed by a 95% confidence level. Within the wake (W2), although the wavelet power around M_2 tidal period keeps standing out, the significant wavelet power as indicated by the 95% confidence level occupies most of the range of St-based period (Fig. 10b). Here, the band of wavelet power around the M_4 period becomes distinct. The cross-wavelet power spectrum between zonal velocities at the two sites shows similar patterns (Fig. 10c) but the significant region concentrates more on the St-based period. The enhanced cross-wavelet power between M_2 and M_4 tidal periods may be associated with the 7.4 and 8.6 h spectral peaks found in the cross-spectral density (Fig. 9), reflecting the intrinsic period of evolution. The averaged phase angle within the St-based period is close to $-\pi/2$ again (not shown). Although the tidal oscillations are the predominant processes, the intrinsic period of the eddy shedding can be recognized when the tidal signals at the wake edge are weak as shown from 19 to 28 August (Fig. 10a). In 19–28 August (marked as yellow boxes in Fig. 10), the significant wavelet power ($>95\%$ confidence level) at W2 (Fig. 10b) and cross-wavelet power (Fig. 10c) along the vicinity of the tidal period within the range of St-based period are not strengthened, which may solely reflect the intrinsic period of the eddy shedding. Therefore, we conclude that the evolution of eddy development may reflect a combination of periods resulting from the

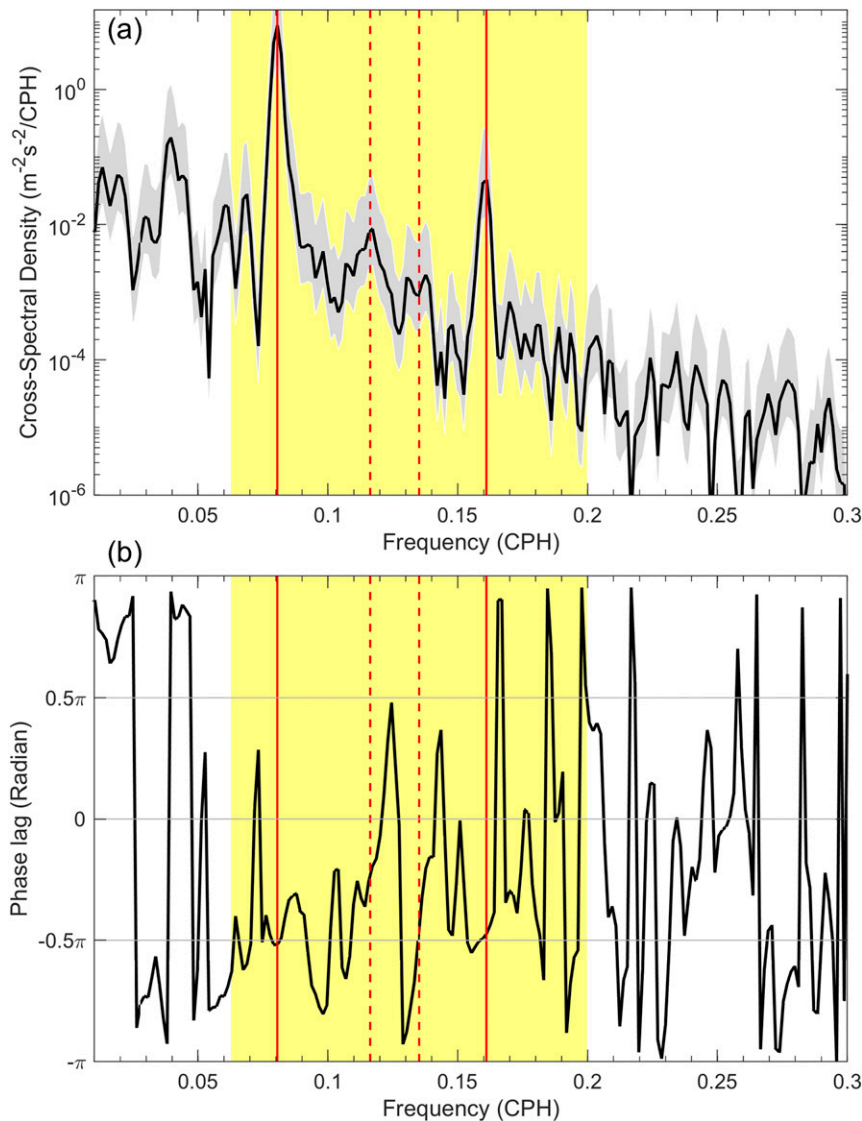


FIG. 9. (a) Cross-spectral density and (b) phase lag measured between zonal velocity averaged over 60–100 m at W1 and zonal velocity averaged over 20–60 m at W2. The yellow shaded areas denote the St-based period (5–16 h). The gray shaded areas in (a) represent the 95% confidence interval. Red solid lines denote spectral peaks measured at 8.05×10^{-2} and 1.61×10^{-1} cph corresponding to M_2 (12.42 h) and M_4 (6.21 h) tidal constituents, respectively. The red dashed lines denote frequencies measured at 1.16×10^{-1} (8.6 h) and 1.35×10^{-1} cph (7.4 h).

incident flow oscillations and the intrinsic time scale regulated by Re–St relationship (Figs. 2c,d).

Observations of Dennis *et al.*'s (1995) in the lee side of the headland show that a tidal component of the upstream mean flow spurs oscillation in the wake of tidal frequency with the resonance effect. The above mechanism could be one of the possible processes to explain our observed wake features. The Re– T diagram corresponding to our Ex1 (blue curve in Fig. 2d) and Ex2 (red curve in Fig. 2d) data shows that T is mostly observed between the M_2 and M_4 tidal periods (dashed

magenta lines). This suggests that the wake period may occur in the M_2 tidal period or M_4 tidal period if the resonance effect occurs because the two periods manifest during the natural period of wake evolution. Following this line of reasoning, the wake is unlikely to occur during a diurnal tidal period because semidiurnal resonance would occur prior to its diurnal counterpart. Tidal ellipses of the three tides reflecting the results of our tidal harmonic analysis (Pawlowicz *et al.* 2002) lend further support to this conclusion (Fig. 4e). The semi-major axis of the M_2 tide at W1 is 0.17 m s^{-1} and is thus

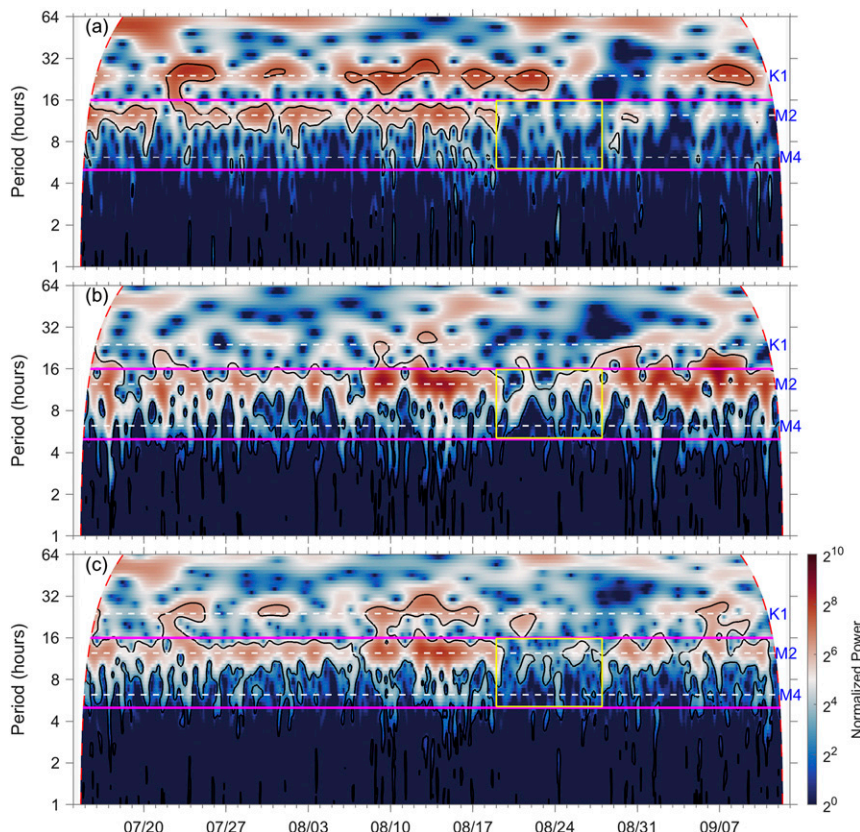


FIG. 10. The wavelet power spectrum for (a) zonal velocity averaged over 60–100 m at W1 and (b) zonal velocity averaged over 20–60 m at W2 using Morlet wavelet, normalized by variance. (c) The cross-wavelet power spectrum between zonal velocity averaged over 60–100 m at W1 and zonal velocity averaged over 20–60 m at W2, normalized by their covariance. The black contours enclose the regions of confidence level larger than 95%. The red dashed lines show the cone of influence. The white dashed lines denote the periods of K_1 , M_2 , and M_4 tides. The magenta lines denote the range of St-based period (5–16 h).

~ 3 times larger than that of the M_4 tide (0.05 m s^{-1}). Inclination angles are respectively positioned 53° and 42° to the north for the M_2 and M_4 tides. Semimajor axes of the M_2 (0.15 m s^{-1}) and M_4 (0.04 m s^{-1}) tides at W2 are comparable to their counterparts at W1. The inclination angles of -60° and -81° for the M_2 and M_4 tides respectively support mooring at W2 southeast of anticyclonic recirculation.

In contrast, the discrepancy in K_1 tidal ellipses observed between the W1 and W2 moorings is significant. The semimajor axis of the K_1 tide at W1 is 0.2 m s^{-1} and thus slightly larger than that of M_2 . However, the K_1 tidal signal nearly vanishes at W2 within the recirculation area and only 5 km east of W1 with its semimajor axis measured at 0.01 m s^{-1} . The K_1 tidal ellipse at S1 outside of the wake presents a similar semimajor axis and orientation (Fig. 4e), illustrating the absence of K_1 tides within the recirculation area. It implies the K_1 tide is not able to form a recirculation while the Green Island acts

as an obstacle to intercept the K_1 tidal signals in its lee. It is notable that the M_2 and M_4 tidal ellipses measured at S1 are predominately of a cross-stream orientation (i.e., perpendicular to the mean flow). Magnitude and orientation values echo numerical results given in Jan et al. (2008) and Chiou et al. (2011) (not shown).

Following the hypothesis of resonance effects raised by Denniss et al. (1995), we further interpret the island wake induced by a large-scale flow modulated by the cross-stream tidal current as the wake forming on the lee side of a cylinder oscillating transversely within a free stream, a classic focus of fluid water tank mechanics experiments. Cross-stream tidal excursion is analogous to the displacement of a cross-stream oscillating cylinder with the opposite sign. According to this scenario, the vortex formation period can be synchronized with the cylinder's oscillating period (Bishop and Hassan 1964; Berger and Wille 1972; Williamson and Roshko 1988), thus eliminating the natural (St-based) period.

Relevant parameters supportive of the occurrence of synchronization include the amplitude ratio A/D and the wavelength ratio λ/D , where A is the oscillating amplitude and $\lambda = UT_e$, T_e is the period of cylinder oscillation. Williamson and Roshko (1988) summarized their water tank experiment results with a diagram of a synchronization region based on the A/D – λ/D plane (Fig. 11). We borrow their diagram to indicate where Green Island is positioned within the synchronization region. In our case, A and T_e are respectively the cross-stream tidal excursion value and tidal period. Tidal excursion A can be computed as

$$u_{\max} T_e / \pi, \quad (3)$$

where u_{\max} is the maximum cross-stream tidal flow, which is determined from the semimajor axis of the tidal ellipse projecting in the cross-stream direction. As a result, u_{\max} is valued at 0.076, 0.1 and 0.013 m s^{-1} for the K_1 , M_2 , and M_4 tides, respectively. According to (3), A is measured as 2.08, 1.42, and 0.093 km for the K_1 , M_2 , and M_4 tides, respectively, corresponding to $A/D = 0.29$, 0.2, and 0.013, respectively, when $D = 7$ km. On the other hand, λ/D is valued at 12.3, 6.39, and 3.2 for the K_1 , M_2 , and M_4 tides, respectively. We present our estimate in an A/D – λ/D diagram as shown in Fig. 11. The red curve separates the synchronization and nonsynchronization regimes. The K_1 and M_4 tides are distinctly and respectively positioned within the nonsynchronization and synchronization regimes. The M_2 tide is positioned close to the separating curve. The slight change in tidal excursion, the mean flow speed U , and the definition of D can modify the regime of the M_2 tide. The corresponding level of uncertainty is difficult to determine given that the error value associated with water tank experiments is also unknown. In addition, the A/D – λ/D diagram classifies different patterns of vortex distributions as illustrated by the schematic diagram given in Fig. 11 pertaining to different regimes. In our observations, the shedding period of the vortex is likely synchronized to a tidal period close to the intrinsic period, but the intrinsic (St-based) period is not eliminated as mentioned in previous water tank experiment (Berger and Wille 1972; Williamson and Roshko 1988). Instead, they can independently coexist as shown in the wavelet spectrum (Fig. 10).

5. Discussion

The wavy thermal front observed along the FSL (Figs. 3 and 5) may be related to vortices of Kelvin–Helmholtz instability within the FSL as shown by the water tank experiment conducted at $\text{Re} = 5000$ (marked

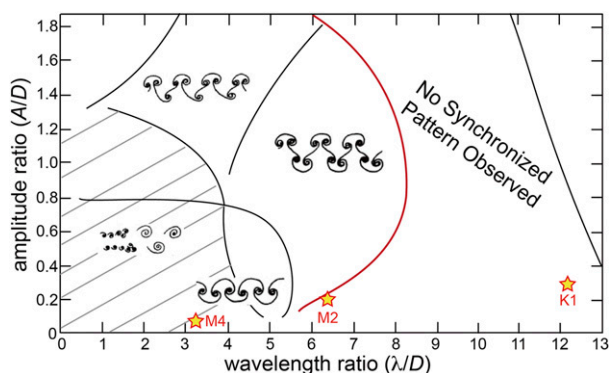


FIG. 11. Synchronization and vortex patterns based on λ/D – A/D diagrams reproduced from Williamson and Roshko (1988). The black curves depict different wake pattern regimes. The red curve separates the diagram into nonsynchronization and synchronization regimes. The stars show the positioning of the K_1 , M_2 , and M_4 tides.

as KHI in Fig. 1b). Returning to moored temperature measurements collected at W1 (red curve) and W2 (black curve) shown in Fig. 4c, the temperature measured at W1 (where the FSL can move around) fluctuates more than that measured at W2 at a small scale. A comparison of the raw temperature (red curve) to the 1-h low-pass-filtered temperature (green curve) reveals that minor oscillations are shaped by tidal variations. Temperature oscillations appear intermittently over a time scale of 0.5–2 h. Relating these results to the quasi-synoptic maps of Ex2 (Fig. 3) reveals that the magnitude of temperature oscillations is more significant when FSL is positioned close to mooring W1 (Fig. 5), for example, stages 1, 5, 8, and 9, where (unperturbed) currents along the western edge are primarily oriented northward. By contrast, these oscillations become weak or disappear when the Kuroshio loops eastward to form recirculation accompanied by FSL migration to the east of mooring W1 (e.g., stage 2 in Fig. 5). Clearly, small-scale temperature oscillations observed at W1 are related to the wavy thermal front observed along the FSL and are revealed by moored velocity measurements as well. A spectral analysis of zonal velocity averaged at 60–100 m for W1 (black curve in Fig. 4d) shows a spectral bump forming over 0.5–3 h (denoted by the green box) that is absent from spectra of zonal velocity averaged at 20–60 m at W2 (red curve in Fig. 4d), as the FSL could not reach mooring W2 in any phase of our ship-based mapping study (Fig. 5). Clearly, the wavy thermal front observed is associated with strong shearing in the FSL.

Unfortunately, detailed dynamics of the wave-like feature observed in the FSL are challenging to identify due to a loss of synopticity and insufficient observation resolutions employed. For instance, we find no obvious

propagation of wave-like features in the FSL when comparing different stages of our ship-based mapping study (Fig. 3). This is presumably the case because the length scale (~ 2 km) of wave-like patterns shown in Fig. 3 covers only ~ 2 times the distance between two adjacent survey lines (~ 1 km) such that their propagation signatures are difficult to recognize due to the Nyquist sampling problem. Indeed, signatures of temperature oscillation at mooring W1 in the FSL would be absent if the wave-like feature did not propagate. To determine the period of oscillation, 6-h high-pass filtered temperatures T_h taken from W1 during ship-based measurement stages 1 and 9 (when the FSL hovers over the mooring site (Fig. 3) because the background current is primarily oriented northward) are shown in Fig. 12. Around stage 1 (Fig. 12a), three nearly sinusoidal oscillations marked as red, green, and blue curves are identifiable and correspond to oscillating periods of 34, 44.5, and 127.8 min, respectively. Phase speeds observed are respectively valued at 0.98, 0.75, and 0.26 m s^{-1} for the red, green, and blue oscillations when a wavelength of 2 km is adopted. Growth in KH instability can only occur when the phase speed is close to the background flow speed where the shear is at a maximum and where instability levels increase at the expense of mean flow energy (Kundu and Cohen 2004). Thus, the phase speed of oscillation should be equal to a specific isotach value measured within a strong shear band (Fig. 5). We find that both the 0.98 m s^{-1} isotach (red curve pertaining to stage 1, Fig. 5) and 0.75 m s^{-1} isotach (green curve pertaining to stage 1, Fig. 5) fall within the strong shear band ($|\xi/f| > 20$) in agreement with conditions of KH instability. This agreement does not occur at the 0.26 m s^{-1} isotach (not shown). While the reason for this outcome is unknown, it could be attributed to the lateral migration of the FSL. Similarly, two nearly sinusoidal oscillations occurring around stage 9 (Fig. 12b) are marked as red and green curves with oscillating periods of 49.8 and 66.6 min, respectively. The phase speeds of red and green oscillations are valued at 0.67 and 0.5 m s^{-1} , respectively. Again, the strong shear band region associated with the FSL includes the two isotachs (Fig. 12b).

The foregoing analyses point to the likelihood of the wavy thermal front observed constituting a likely form of Kelvin–Helmholtz instability generated by strong shearing at the FSL between the free stream and wake vortex. Such a scenario is rarely observed in geophysical wakes but has long been observed in cylinder wakes in laboratory settings (e.g., Prasad and Williamson 1997). Though it remains arguable whether the two wakes present sufficient similarities to draw a direct link, a simple comparison and discussion is provided here. Water tank experiments demonstrate that the separating shear

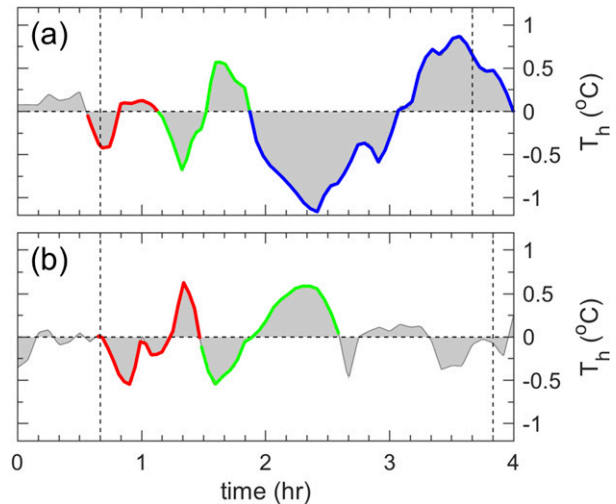


FIG. 12. The 6-h high-pass-filtered temperatures T_h measured from W1 during ship-based measurement periods of (a) stage 1 and (b) stage 9. Nearly sinusoidal oscillations shown in (a) are presented as red, green, and blue curves covering periods of 34, 44.5, and 127.8 min, respectively. Nearly sinusoidal oscillations in (b) are presented as red and green curves covering periods of 49.8 and 66.6 min, respectively.

layer from a cylinder becomes unstable when $Re \sim O(10^3-10^4)$ (Fig. 11 in Prasad and Williamson 1997). However, previous island wake studies define Re as $O(10^2)$ as summarized in Fig. 2c, suggesting an absence of secondary shear instability. We argue that the value of Re in the scale wake may have been underestimated (at least for Green Island). To further examine the range of Re of the Green Island wake, the dependence of the time scale of secondary shear instability on the value of Re is explored. In summarizing the results of water tank experiments, Prasad and Williamson (1997) defined the empirical relationship as

$$\frac{f_{SL}}{f_K} = 0.0235 \times Re^{0.67}, \quad (4)$$

where f_{SL} and f_K are respectively the frequency of the oscillating wake and shear layer instability. The value of f_{SL}/f_K is 6–25 for a period of wake oscillation of 12.42 h (M_2 tide) and for a shear layer instability period of 0.5–2 h. The consequent Re value ranges from 4000 to 30 000. Alternatively, Re ranges from 1000 to 10 000 when the period of wake oscillation is 6.21 h (M_4 tide). As a result, the corresponding horizontal eddy viscosity value ν_h ranges from 0.2 to $7 \text{ m}^2 \text{ s}^{-1}$ ($U = 1 \text{ m s}^{-1}$ and $D = 7000 \text{ m}$) and is thus much smaller than levels observed in the open ocean, which vary from 10^2 to $10^5 \text{ m}^2 \text{ s}^{-1}$ (Apel 1987). The effects of ν_h in the open ocean on submesoscale processes may be questionable. Recently, Nencioli et al. (2013) provided an in situ

estimation showing that ν_h at submesoscale fronts mostly ranges from 0.4 to $5 \text{ m}^2 \text{ s}^{-1}$, which is in agreement with the cases presented here. Indeed, the “clear” von Kármán vortex street appearing at $\text{Re} \sim O(10^2)$ in the water tank (Fig. 1a) has rarely been observed in the Green Island wake. Instead, the noisy and distorted wake shown from the visualization of wake patterns at $\text{Re} \sim O(10^3)$ in Fig. 1b was frequently captured by satellite images as shown in Fig. 1c.

6. Conclusions

The presence of a small island in the strong mean flow leads to the formation of complex wake systems primarily presenting an alternate shedding of positive and negative vortices. The dynamics underlying oceanic wake flows are primarily examined through an experimental investigation of circular cylinder wakes in laboratory tanks and numerical domains, where a steady and uniform upstream velocity is typically sustained. Whether the cylinder wake formed in a water tank is consistent with an island wake in the vast and complex ocean must be verified with field observations. In this study, oceanic vortex evolution on the lee side of Taiwan’s Green Island ($\sim 7 \text{ km}$ in diameter), where the Kuroshio flows at a speed of $1\text{--}1.5 \text{ m s}^{-1}$, is examined with in situ observations and is compared to patterns observed from previous idealized water tank experiments.

The combination of a strong current with a small island points to a wake presenting high levels of vorticity, that is, a high Ro . Two ship-based experiments were designed to observe the flow and hydrographic evolution in near and far wakes, respectively. Two sets of moored ADCP data measured from the near wake were also used to supplement ship-based observations. In the near wake, recirculation with a relative vorticity value of $\zeta \sim 20f$ forms and subsequently sheds at a combination of periods resulting from the tidal oscillations (M_2 or M_4 tides) and the intrinsic time scale regulated by $\text{Re}\text{--}\text{St}$ relationship. The tidal oscillations are the predominant processes. Our analyses suggest that an island encountering the Kuroshio with periodic and cross-stream tidal excursion is analogous to a cross-stream oscillating cylinder, a classic and extensively studied focus of fluid mechanics. As a consequence, the shedding period of the vortex is synchronized with a tidal period occurring close to its intrinsic period. This is an instructive finding, as ocean currents consist of quasi-steady subtidal and periodic tidal components rather than a steady flow due to the ubiquity of tides. Previous numerical studies of island wakes, for example, Dong et al. (2007), Huang et al. (2014) and Liu and Chang (2018), neglect the crucial role of tidal effects.

The free shear layer in the near wake characterized by an $\sim 30f$ relative vorticity band (2 km in width) and a zigzag-shaped thermal front was found to develop between the Kuroshio and the recirculation area. The frontal wave measured over $0.5\text{--}2 \text{ h}$ echoes patterns of Kelvin–Helmholtz instability, which are related to a high Re . In the vertical area, the tilting of the free shear layer is related to the vertical structure of the Kuroshio’s velocity core curving toward the island’s leeward side in a vertically asymmetric manner. We found that the tilting of the isotach can enhance the vertical shear and (potentially) turbulence mixing immediately after the threshold for vertical shear instability is reached in agreement with Chang et al. (2013) and Liu and Chang (2018). For the far wake, repeated cross-wake surveys suggest that cyclonic and anticyclonic eddies alternatively form in a period close to the period of M_2 tide formation consistent with near-wake measurements. Our repeated along-wake surveys show that a cyclonic eddy sheds downstream at a speed of 0.35 m s^{-1} and at $1/3$ of the upstream current speed from the near wake. From a comparison of our observations to previous results obtained from water tank experiments we infer that the value of Re for the submesoscale wake regime is $O(10^3)$ and has long been underestimated in previous wake studies.

Oceanic island wakes have been the subject of extensive research given their significant role in the energy cascade observed from large-scale flows to small-scale turbulence dissipation and mixing (Barkley 1972; Farmer et al. 2002; Hasegawa et al. 2004; Chang et al. 2013), due to their critical influence on surrounding biological environments (Doty and Oguri 1956; Heywood et al. 1990; Hasegawa et al. 2009) and even on the development of renewable energy (Hsu et al. 2015). All assessments of the above environmental impacts must examine specific processes that occur in a wake. Our observations suggest that vortex shedding in the island wake at a high Ro within a mean flow (e.g., a western boundary current) may frequently be subjected to tidal synchronization since its intrinsic period is recorded as $O(0.1\text{--}1)$ day and typically occurs close to a tidal period. This differentiates oceanic wakes from cylinder wakes observed in laboratory settings and other geophysical wakes, as associated tides are ubiquitous in the ocean. The free shear layer of the near wake characterized by a very strong relative vorticity value of $\sim 30f$ accompanied by a wavy thermal front is demonstrated for the first time. Presumably, the wavy thermal front observed could be a result of KH instability as suggested by water tank experiments conducted at a high Re . To the best of our knowledge, this may be the first paper to propose the above two important features of island wakes on the

basis of observations of the ocean field. Applications and further studies of these results concerning tidal synchronization and strong patterns of shear instability are encouraged.

Acknowledgments. The authors thank the crew and officers of the R/V *Ocean Researcher 3* for supporting our experiments. We also thanks Wei-Ting Hung, Wen-Hwa Her, Sin-Ya Jheng, Hsiang-Chih Hsieh, and Wen-Hui Lee for mooring preparation and operation. Bee Wang, Wan-Ting Hsieh, and Sin Huei Yu assisted with UCTD operations. Dr. Shiao-Yih Tzang provided the ADCP needed at W1. Comments from two anonymous reviewers improved the preliminary manuscript markedly. MC was supported by Taiwan's Ministry of Science and Technology (MOST) through Grants 103-2611-M-002-018, 105-2611-M-002-012, and 107-2611-M-002-015. SJ and VM were supported with MOST Grants 101-2611-M-002-018-MY3, 103-2611-M-002-011, and 105-2119-M-002-042. YC was supported by the CWB of Taiwan through Grant 1062076C. We thank the MOST Ocean Data Bank for providing historic ship-based ADCP and bathymetry data (<http://www.odn.ntu.edu.tw/odn/>). We use the wavelet tools provided by Grinsted et al. (2004) (code available at <http://noc.ac.uk/using-science/crosswavelet-wavelet-coherence>) to compute the wavelet and cross-wavelet transforms. Data drawn from ship-based and moored measurements used to produce the figures presented in this article can be obtained from <https://doi.org/10.5281/zenodo.2560903>.

REFERENCES

- Apel, J. R., 1987: *Principles of Ocean Physics*. Academic Press, 631 pp.
- Barkley, R. A., 1972: Johnston's atoll's wake. *J. Mar. Res.*, **30**, 201–216.
- Berger, E., and R. Wille, 1972: Periodic flow phenomena. *Annu. Rev. Fluid Mech.*, **4**, 313–340, <https://doi.org/10.1146/annurev.fl.04.010172.001525>.
- Bishop, R. E. D., and A. Y. Hassan, 1964: The lift and drag forces on a circular cylinder oscillating in a flowing fluid. *Proc. Roy. Soc. London*, **277A**, 51–75, <https://doi.org/10.1098/rspa.1964.0005>.
- Black, K. P., and S. L. Gay, 1987: Eddy formation in unsteady flows. *J. Geophys. Res.*, **92**, 9514–9522, <https://doi.org/10.1029/JC092iC09p09514>.
- Caldeira, R. M. A., and P. Sangrà, 2012: Complex geophysical wake flows. *Ocean Dyn.*, **62**, 683–700, <https://doi.org/10.1007/s10236-012-0528-6>.
- Chang, M.-H., T.-Y. Tang, C.-R. Ho, and S.-Y. Chao, 2013: Kuroshio-induced wake in the lee of Green Island off Taiwan. *J. Geophys. Res. Oceans*, **118**, 1508–1519, <https://doi.org/10.1002/jgrc.20151>.
- , S.-Y. Jheng, and R.-C. Lien, 2016: Trains of large Kelvin-Helmholtz billows observed in the Kuroshio above a seamount. *Geophys. Res. Lett.*, **43**, 8654–8661, <https://doi.org/10.1002/2016GL069462>.
- , S. Jan, V. Mensah, M. Andres, L. Rainville, Y.-J. Yang, and Y.-H. Cheng, 2018: Zonal migration and transport variations of the Kuroshio east of Taiwan induced by eddy impingements. *Deep-Sea Res. I*, **131**, 1–15, <https://doi.org/10.1016/j.dsr.2017.11.006>.
- Chiou, M. D., S. Jan, J. Wang, R. C. Lien, and H. Chien, 2011: Sources of baroclinic tidal energy in the Gaoping Submarine Canyon off southwestern Taiwan. *J. Geophys. Res.*, **116**, C12016, <https://doi.org/10.1029/2011JC007366>.
- Coutis, P., and J. Middleton, 1999: Flow-topography interaction in the vicinity of an isolated, deep ocean island. *Deep-Sea Res. I*, **46**, 1633–1652, [https://doi.org/10.1016/S0967-0637\(99\)00007-2](https://doi.org/10.1016/S0967-0637(99)00007-2).
- Denniss, T., J. H. Middleton, and R. Manasseh, 1995: Recirculation in the lee of complicated headlands: A case study of Bass Point. *J. Geophys. Res.*, **100**, 16 087–16 101, <https://doi.org/10.1029/95JC01279>.
- Dong, C., J. C. McWilliams, and A. F. Schepetkin, 2007: Island wakes in deep water. *J. Phys. Oceanogr.*, **37**, 962–981, <https://doi.org/10.1175/JPO3047.1>.
- Doty, M. S., and M. Oguri, 1956: The island mass effect. *ICES J. Mar. Sci.*, **22**, 33–37, <https://doi.org/10.1093/icesjms/22.1.33>.
- Farmer, D., R. Pawlowicz, and R. Jiang, 2002: Tilting separation flows: A mechanism for intense vertical mixing in the coastal ocean. *Dyn. Atmos. Oceans*, **36**, 43–58, [https://doi.org/10.1016/S0377-0265\(02\)00024-6](https://doi.org/10.1016/S0377-0265(02)00024-6).
- Grinsted, A., J. C. Moore, and S. Jevrejeva, 2004: Application of the cross wavelet transform and wavelet coherence to geophysical time series. *Nonlinear Processes Geophys.*, **11**, 561–566, <https://doi.org/10.5194/npg-11-561-2004>.
- Hasegawa, D., H. Yamazaki, R. G. Lueck, and L. Seuront, 2004: How islands stir and fertilize the upper ocean. *Geophys. Res. Lett.*, **31**, L16303, <https://doi.org/10.1029/2004GL020143>.
- , M. R. Lewis, and A. Gangopadhyay, 2009: How islands cause phytoplankton to bloom in their wakes? *Geophys. Res. Lett.*, **36**, L20605, <https://doi.org/10.1029/2009GL039743>.
- Heywood, K. J., E. D. Barton, and J. H. Simpson, 1990: The effects of flow disturbance by an oceanic island. *J. Mar. Res.*, **48**, 55–73, <https://doi.org/10.1357/002224090784984623>.
- , D. P. Stevens, and G. R. Bigg, 1996: Eddy formation behind the tropical island of Aldabra. *Deep-Sea Res. I*, **43**, 555–578, [https://doi.org/10.1016/0967-0637\(96\)00097-0](https://doi.org/10.1016/0967-0637(96)00097-0).
- Hsu, P.-C., M.-H. Chang, C.-C. Lin, S.-J. Huang, and C.-R. Ho, 2017: Investigation of the island-induced ocean vortex train of the Kuroshio Current using satellite imagery. *Remote Sens. Environ.*, **193**, 54–64, <https://doi.org/10.1016/j.rse.2017.02.025>.
- Hsu, T. W., J. M. Liao, S. J. Liang, S. Y. Tzang, and D. J. Doong, 2015: Assessment of Kuroshio current power test site of Green Island, Taiwan. *Renew. Energy*, **81**, 853–863, <https://doi.org/10.1016/j.renene.2015.03.089>.
- Huang, S.-J., C.-R. Ho, S.-L. Lin, and S.-J. Liang, 2014: Spatial-temporal scales of Green Island wake due to passing of the Kuroshio current. *Int. J. Remote Sens.*, **35**, 4484–4495, <https://doi.org/10.1080/01431161.2014.916047>.
- Jan, S., R.-C. Lien, and C.-H. Ting, 2008: Numerical study of baroclinic tides in Luzon Strait. *J. Oceanogr.*, **64**, 789–802, <https://doi.org/10.1007/s10872-008-0066-5>.
- , V. Mensah, M. Andres, M.-H. Chang, and Y.-J. Yang, 2017: Eddy-Kuroshio interactions: Local and remote effects. *J. Geophys. Res. Oceans*, **122**, 9744–9764, <https://doi.org/10.1002/2017JC013476>.
- Kundu, P. K., and I. M. Cohen, 2004: *Fluid Mechanics*. 3rd ed. Academic Press, 497 pp.
- Liu, C.-H., and M.-H. Chang, 2018: Numerical studies of submesoscale island wakes in the Kuroshio. *J. Geophys. Res. Oceans*, **123**, 5669–5687, <https://doi.org/10.1029/2017JC013501>.

- Molemaker, J., J. McWilliams, and W. Dewar, 2015: Submesoscale instability and generation of mesoscale anticyclones near a separation of the California Undercurrent. *J. Phys. Oceanogr.*, **45**, 613–629, <https://doi.org/10.1175/JPO-D-13-0225.1>.
- Neill, S. P., and A. J. Elliott, 2004: Observations and simulations of an unsteady island wake in the Firth of Forth, Scotland. *Ocean Dyn.*, **54**, 324–332, <https://doi.org/10.1007/s10236-003-0084-1>.
- Nencioli, F., F. d'Ovidio, A. M. Doglioli, and A. A. Petrenko, 2013: In situ estimates of submesoscale horizontal eddy diffusivity across an ocean front. *J. Geophys. Res. Oceans*, **118**, 7066–7080, <https://doi.org/10.1002/2013JC009252>.
- Pawlowicz, R., B. Beardsley, and S. Lentz, 2002: Classical tidal harmonic analysis including error estimates in MATLAB using T_TIDE. *Comput. Geosci.*, **28**, 929–937, [https://doi.org/10.1016/S0098-3004\(02\)00013-4](https://doi.org/10.1016/S0098-3004(02)00013-4).
- Perfect, B., N. Kumar, and J. J. Riley, 2018: Vortex structures in the wake of an idealized seamount in rotating, stratified flow. *Geophys. Res. Lett.*, **45**, 9098–9105, <https://doi.org/10.1029/2018GL078703>.
- Prasad, A., and C. H. K. Williamson, 1997: The instability of the shear layer separating from a bluff body. *J. Fluid Mech.*, **333**, 375–402, <https://doi.org/10.1017/S0022112096004326>.
- Provansal, M., C. Mathis, and L. Boyer, 1987: Bénard-von Kármán instability: Transient and forced regimes. *J. Fluid Mech.*, **182**, 1–22, <https://doi.org/10.1017/S0022112087002222>.
- Signell, R. P., and W. R. Geyer, 1991: Transient eddy formation around headlands. *J. Geophys. Res.*, **96**, 2561–2575, <https://doi.org/10.1029/90JC02029>.
- Teague, W. J., P. A. Hwang, G. A. Jacobs, J. W. Book, and H. T. Perkins, 2005: Transport variability across the Korea/Tsushima Strait and the Tsushima Island Wake. *Deep-Sea Res. II*, **52**, 1784–1801, <https://doi.org/10.1016/j.dsr2.2003.07.021>.
- Torrence, C., and G. P. Compo, 1998: A practical guide to wavelet analysis. *Bull. Amer. Meteor. Soc.*, **79**, 61–78, [https://doi.org/10.1175/1520-0477\(1998\)079<0061:APGTWA>2.0.CO;2](https://doi.org/10.1175/1520-0477(1998)079<0061:APGTWA>2.0.CO;2).
- Williamson, C. H. K., 1996a: Vortex dynamics in the cylinder wake. *Annu. Rev. Fluid Mech.*, **28**, 477–539, <https://doi.org/10.1146/annurev.fl.28.010196.002401>.
- , 1996b: Three-dimensional wake transition. *J. Fluid Mech.*, **328**, 345–407, <https://doi.org/10.1017/S0022112096008750>.
- , and A. Roshko, 1988: Vortex formation in the wake of an oscillating cylinder. *J. Fluids Struct.*, **2**, 355–381, [https://doi.org/10.1016/S0889-9746\(88\)90058-8](https://doi.org/10.1016/S0889-9746(88)90058-8).
- , and G. L. Brown, 1998: A series in $1/\sqrt{Re}$ to represent the Strouhal-Reynolds number relationship of the cylinder wake. *J. Fluids Struct.*, **12**, 1073–1085, <https://doi.org/10.1006/jfls.1998.0184>.
- Wolanski, E., and W. M. Hamner, 1988: Topographically controlled fronts in the ocean and their biological influence. *Science*, **241**, 177–181, <https://doi.org/10.1126/science.241.4862.177>.
- Zheng, Q., H. Lin, J. Meng, X. Hu, Y. T. Song, Y. Zhang, and C. Li, 2008: Sub-mesoscale ocean vortex trains in the Luzon Strait. *J. Geophys. Res.*, **113**, C04032, <https://doi.org/10.1029/2008JC005065>.